Journal of Fluids and Structures 120 (2023) 103895

Contents lists available at ScienceDirect

Journal of Fluids and Structures

journal homepage: www.elsevier.com/locate/jfs

Fluidelastic modeling of a weathercock stabilization in a uniform flow

Ariane Gayout [a], Ármann Gylfason [b], Nicolas Plihon [a,*], Mickaël Bourgoin [a]

[a] Univ Lyon, ENSL, CNRS, Laboratoire de Physique, Lyon, F-69342, France
[b] Department of Engineering, Reykjavik University, Menntavegur 1, Reykjavik, IS-102, Iceland

ARTICLE INFO

Article history:
Received 30 June 2022
Received in revised form 8 March 2023
Accepted 14 April 2023
Available online xxxx

MSC:
74F10
70K25

Keywords:
Time domain analysis
Aerodynamics

ABSTRACT

The relaxation dynamics of a weathercock free-to-rotate, in the presence of a uniform flow, as it aligns with the flow direction, is investigated experimentally in a wind-tunnel. The dynamics is observed to conveniently follow a damped harmonic oscillator behavior. At first order, the frequency is set by the aerodynamic coefficients. We show that a quasi static approach fails to precisely describe the relaxation dynamics and that non-stationary corrections are required to model the dynamics. A first strategy is to introduce added mass, added stiffness and added damping to the quasi-static approximation, following what is usually done in the context of vortex-induced vibrations. A second strategy is to introduce empirical corrections, whose scaling is obtained from the analysis of the experimental data. Finally, these two strategies are compared and we discuss the physical interpretations of the non-stationary corrections.

1. Introduction

Flows and wind in particular have the particularity of bringing objects to life, by breathing movement onto them. A good example for this is how wind makes buildings sing (Berhault, 1977) and leaves whistle (Fegeant, 1999a,b) in the audible spectrum, also known as wind-induced vibrations. The description of the dynamics of these objects moving in a flow requires unsteady aerodynamics models, that have been extensively developed over the last century due to their importance in aircraft design, prediction of aeroelastic stability, or development of control strategies, and with the recent emergence of energy harvesters based on unsteady aerodynamics (Lu et al., 2019; Wu et al., 2021; Allen and Smits, 2001; Olivieri et al., 2017; Tavallaeinejad et al., 2021). The field of unsteady aerodynamics dates back to the pioneering works of Wagner (1925), Theodorsen (1935) and their variants (von Kármán and Sears, 1938). Theodorsen model includes added-mass forces and idealized wake vorticity to incompressible thin airfoils in two-dimensions, assuming inviscid flow and infinitesimal motions. Wagner's model belongs to the class of indicial response models (Truong and Tobak, 1990), where the lift coefficients are computed as a response to a given time dependent angle of attack, knowing the indicial response to a step function of the angle of attack. These models have been extensively studied and developed due to the importance of unsteady dynamics for various applications (see for instance the reviews (Peters, 2008; McCroskey, 1982). On the other hand, the ever-increasing complexity of data obtained using modern numerical simulations or experimental characterization led to the development of reduced-order models expressed in the form of state–space representation (see Brunton et al. (2013), Taha et al. (2014) for detailed discussions). The reduced-order models are thus usually built upon parameter identification from experimental or numerical data. Note that Theodorsen's model can be recast into the

* Corresponding author.
E-mail address: nicolas.plihon@ens-lyon.fr (N. Plihon).

https://doi.org/10.1016/j.jfluidstructs.2023.103895
0889-9746/

state–space representation (Brunton and Rowley, 2013). The use of quasi-static *versus* unsteady aerodynamic modeling is usually quantified using the reduced velocity Ur or equivalently the reduced frequency k. For a body oscillating at a frequency f, the reduced velocity is defined as $U/(fD)$ with D the characteristic dimension of the object and U the mean wind velocity. The reduced frequency is defined as $k = \pi/\mathrm{Ur}$. When $\mathrm{Ur} \gg 1$ ($\mathrm{Ur} > 20$ in practice (Blevins, 1990)), a quasi-static approach usually becomes relevant, using for instance drag and lift coefficients as traditionally measured in wind-tunnels for static objects and steady wind conditions. While criteria for the validity of quasi-static approaches have been proposed in oscillatory motion such as flapping flight (Taha et al., 2014), no consensus has yet been found for general application of quasi-static approximation in aeroelasticity (Haddadpour and Firouz-Abadi, 2006).

In this article, we investigate wind induced oscillations in a system which is aerodynamically stable, but which exhibits damped oscillations in the path towards its final stable equilibrium state when initially put far from equilibrium. More specifically, we consider the dynamics of a simple free-to-rotate object, a balanced disk pendulum, subject to a uniform flow. When the pendulum is initially placed with the disk facing the wind, it experiences self-oscillations until it eventually reaches its final natural equilibrium position aligned with the wind, similar to the response of a weathercock to a cross flow. We address here the question of the dynamics of the weathercock through its path to equilibrium, and the relevance of quasi-static or unsteady descriptions of the dynamics. Studying a balanced pendulum was motivated by features of the dynamics of a weighted pendulum immersed in a flow (Obligado et al., 2013; Gayout et al., 2021) for which the equilibrium position is set by a balance between the torque of the weight and the aerodynamic torque. The non-monotonic dependency of the aerodynamic coefficients of an inclined circular disk facing a uniform flow (Flachsbart, 1932), especially at the stall angle, then leads to a multistable system. Studying the relaxation of such a weighted pendulum would thus lead to strongly non-linear dynamics — and the estimate of the validity of quasi-static approaches would then be an extremely difficult task due to the static non-linearities and the possible occurrence of strong dynamic stall (Corke and Thomas, 2015). Contrary to a weighted pendulum, the balanced pendulum has no prescribed natural frequency f which can be used *a priori* to estimate the reduced velocity Ur of the system in order to know beforehand the importance of non-stationary effects. As we will see, the natural self-oscillating frequency is itself an aerodynamic response whose order of magnitude can be reasonably estimated based on the quasi-static normal drag coefficient, while the overall dynamics still requires to account for non-stationary corrections. This article is organized as follows. The experimental setup, consisting of a balanced pendulum immersed in a wind tunnel, is described in Section 2. Signal analysis of the measurements of the time evolution of the relaxation of the weathercock towards its equilibrium position, and of their interpretation is also detailed in Section 2. Non-stationary corrections are then introduced in Section 3. These corrections are compared in Section 4, while the physical interpretations of each of the correction parameters are discussed in the same section. Finally, Section 5 concludes this article.

2. Material and methods

2.1. Experimental setup

A schematic view of the experimental setup is provided in Fig. 1. A balanced disk pendulum, acting like a weathercock, is placed in a wind tunnel. The disk pendulum consists of a thin disk of diameter d, surface area $S = \pi d^2/4$, and thickness e, made of aluminum or Vivak® and glued to a sanded saw blade of length 31 cm. The pendulum is balanced by coinciding the pivot with the center of mass. Frictionless rotation is ensured by an air bushing (OAVTB16i04 from OAV Labs) equipped with a contact-less rotary encoder that records the angular position α of the blade with minimal friction (DS-25, 17-bit digital encoder from Netzer). The typical length L between the center of mass and the center of the disk is 10 cm. In order to vary the moment of inertia of the weathercock, the blade can be weighted on the opposite side to the disk with a thin circular magnet, aligned with the wind. In this article, we investigate the influence of the disk diameter d, the length L, the moment of inertia J on the dynamics of the weathercock relaxation. As discussed in Section 4, the influence of these parameters is understood using a single dimensionless parameter, the reduced velocity, defined in Eq. (8). As further discussed below, for moderate wind velocities, the magnet also allows to non-intrusively impose the initial out-of-equilibrium position of the weathercock and release it on demand. Table 1 summarizes the various parameters used in the experiments presented in this article.

The wind tunnel in which the weathercock is placed is a closed-loop wind tunnel with a square test section of $51\times51\,\mathrm{cm}^2$. The turbulence rate of the wind tunnel (defined as the ratio of the velocity standard deviation to the mean) is about 2% after the flow has been conditioned through a 6 mm honeycomb. The experiment is conducted with the weathercock in the center of the wind tunnel so that the dynamics of the weathercock is not affected by effects from the walls.

In order to carry a statistically significant characterization of the return to equilibrium of the weathercock, several realizations are repeated for each set of weathercock parameters (according to Table 1) and for different mean wind velocities.

The exact same protocol is followed for all these experimental realization. First, the weathercock is set at the vertical ($\alpha = 90°$). This is achieved either using the magnet and a coil placed below the test section of the wind tunnel (see Fig. 1 or manually using a stick. Then, the flow velocity is increased to its desired test value. The weathercock is finally released (by turning off the magnetic field or removing the stick) and left free to oscillate and to reach its final equilibrium position,

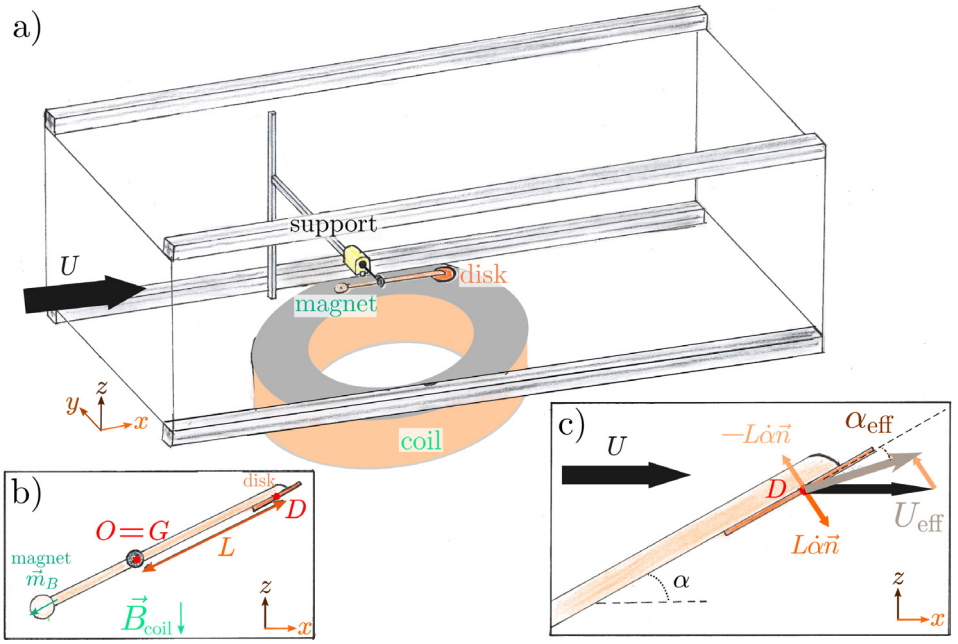

Fig. 1. (a) Experimental setup showing the test section of the wind-tunnel, the pendulum made of a thin disk and the coil for setting the pendulum to the vertical. (b) Details on the pendulum for setting the initial position with the coil. (c) Definition of the effective flow velocity U_{eff} and effective angle of attack α_{eff} acting on the moving disk.

Table 1
Physical characteristics of the different weathercocks used in the experiment. Each disk enables for two sets of experiments, one with a magnet at the blade's opposite end and the other without. Al stands for aluminum.

Diameter d_{disk} (cm)	3	4	5	6	8	9	10
Material	Al	Al	Al	Al	Al	Vivak®	Vivak®
Thickness e (mm)	0.3	0.3	0.3	0.3	0.3	0.6	0.6
Distance L (cm)	13.5	13.8	13.3	12.9	11.8	12.5	12.1
Inertia J (kg cm^2)	1.34	1.57	1.66	1.89	2.24	2.57	2.90
Equivalent Ur	91.2	55.0	36.9	27.8	17.8	14.6	12.8
Equivalent k	0.034	0.057	0.085	0.11	0.18	0.22	0.25
L with magnet (cm)	17.4	17.5	17.3	16.9	16.2	16.5	16.0
J with magnet (kg cm^2)	2.36	2.63	2.86	3.25	3.95	4.31	4.82
Equivalent Ur	107	63.3	42.5	31.8	20.1	16.5	14.3
Equivalent k	0.029	0.050	0.074	0.10	0.16	0.19	0.22

which by static considerations is at the horizontal. Note, that the maximum available magnetic torque limits the magnetic release to low wind velocities (typically $U < 2\,\text{m s}^{-1}$ for the 6 cm disk). This protocol is then repeated for about 10 times for around 8 to 14 values of U for each of the 14 weathercock configurations, leading to 751 independent realizations of the relaxation dynamics, which are analyzed in the following. The magnet being a 30 mm in diameter, 1 mm thick NdFeB disk magnet, its cross section seen by the flow is very small. The aerodynamic contribution of the blade and of the magnet will thus be neglected.

A typical time series obtained following the above-detailed protocol is shown in Fig. 2(a). This signal shows that the weathercock dynamics resembles that of a damped harmonic oscillator, sinusoidal oscillations modulated by an exponential attenuation as evidenced in Fig. 2(b). This signal can be parameterized by two characteristic times, its period $T = 2\pi/\omega$ and its attenuation time $\tau = 2/\beta$, with ω the pulsation of oscillation and β the damping coefficient. The weathercock dynamics could then be described by a simple damped harmonic oscillator equation:

$$\ddot{\alpha} + \beta\dot{\alpha} + \omega^2\alpha = 0 \tag{1}$$

This is not trivial, as the overall aerodynamic forces acting on the weathercock have complex angular dependencies, as illustrated in Fig. 2(c) which represents the normal static drag coefficient $C_{N_{\text{st}}}(\alpha)$ of a fixed inclined disk as a function of the angle of attack (Flachsbart, 1932). We show in the next sub-section that the damped harmonic oscillator behavior is qualitatively expected in a quasi-static description of the aerodynamics of the weathercock in the limit of small oscillations (more precisely in the range of linearity of $C_{N_{\text{st}}}(\alpha)$, *i.e.* for $\alpha \in [-40°; 40°]$). In Section 3 we will show however that a quantitative description requires non-stationary aerodynamic effects to be accurately accounted for.

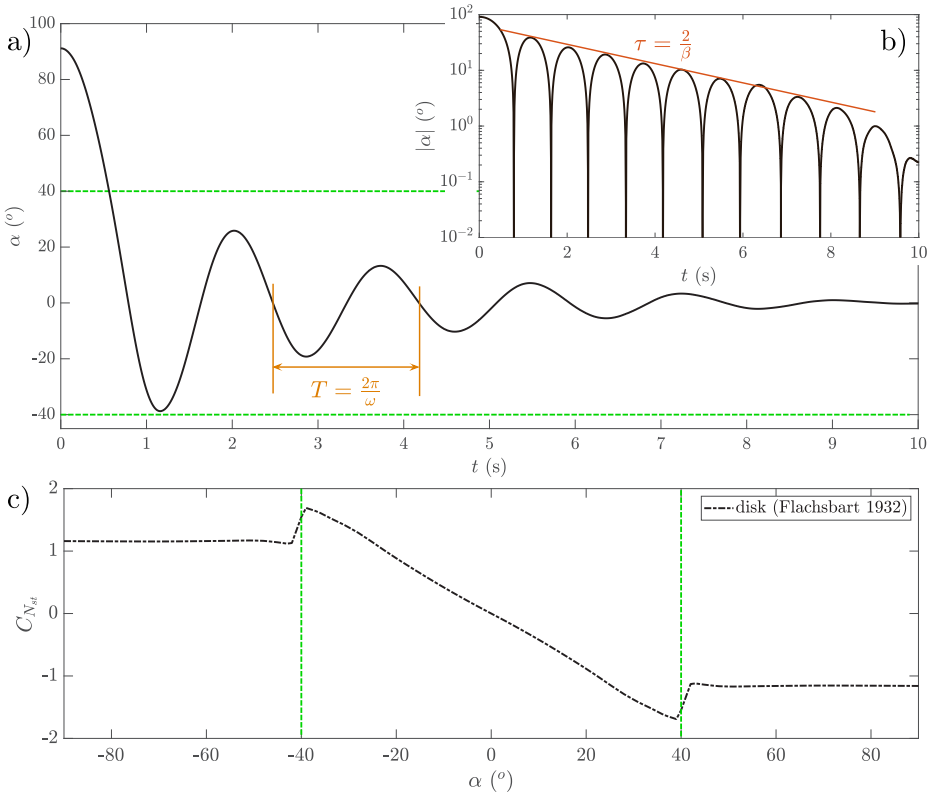

Fig. 2. (a) Example of an experimental signal: the pendulum is set to the vertical and left to oscillate ($d_{disk} = 4$ cm, $J = 2.63$ kg cm^2, and $U = 3$ m s^{-1}). (b) Semi-log presentation of the signal amplitude over time. A pulsation ω can be defined from the period T of oscillation and a damping coefficient β can be extracted from the exponential decrease of amplitude of characteristic time τ. (c) Static C_N coefficient for a disk (Flachsbart, 1932), stall is represented by the dashed green lines.

2.2. Quasi-static momentum equation

In the absence of any weight and any external forcing other than the aerodynamic forces on the disk, the momentum equation governing the weathercock dynamics can be written as:

$$J\ddot{\alpha} = \Gamma_{aero}(t, \alpha, \dot{\alpha}) \tag{2}$$

with Γ_{aero} the instantaneous aerodynamic torque. Note that in a fully non-stationary situation the dependency of aerodynamic quantities as Γ_{aero} may depend on higher order temporal derivatives of the angular dynamics $\alpha(t)$ (added-mass effects, further discussed in the sequel, involve for instance acceleration dependent corrections). For the simplicity of notations we shall however only write $f(t, \alpha, \dot{\alpha})$ when referring to any instantaneous quantity f eventually subject to non-stationary aerodynamic effects.

In the range of Reynolds numbers Re investigated here (i.e. between 10^3 and 10^4, based on the mean wind velocity and the disk diameter, the aerodynamic coefficients are Re-independent. It is convenient to introduce the normal aerodynamic coefficient C_N as $C_N = -C_L \sin(\alpha) + C_D \cos(\alpha)$, with C_L and C_D being respectively the lift and drag coefficients. A standard expression for Γ_{aero} based on dimensional analysis then reads $\Gamma_{aero}(\alpha(t), t) = \frac{1}{2}\rho S U^2 L C_N(\alpha(t), t)$, with ρ the air density, and the notation $\alpha(t)$ refers to non stationary mechanisms depending upon α, $\dot{\alpha}$ and $\ddot{\alpha}$. We stress here that the flow velocity and the angle of attack need to be corrected to account for the actual relative velocity between the disk and the mean stream (Chiereghin et al., 2019), resulting in an effective flow velocity U_{eff} and an effective angle of attack α_{eff} (see Fig. 1c):

$$\begin{cases} U_{\text{eff}}^2 &= U^2 + 2LU\dot{\alpha}\sin(\alpha) + L^2\dot{\alpha}^2 \\ \alpha_{\text{eff}} &= \alpha + \arctan\left(\dfrac{L\dot{\alpha}\cos(\alpha)}{U + L\dot{\alpha}\sin(\alpha)}\right) \end{cases} \tag{3}$$

A first approximation for the expression of normal drag coefficient $C_N(\alpha_{\text{eff}}(t), t)$ is to use its static value $C_{N_{st}}(\alpha_{\text{eff}})$, which is tabulated in the literature for static inclined disks (Flachsbart, 1932), and is displayed in Fig. 2(c). The quasi-static

weathercock dynamics then follows the equation:

$$J\ddot{\alpha} = \frac{1}{2}\rho S L U_{\text{eff}}^2 C_{N_{st}}(\alpha_{\text{eff}}(t)) \tag{4}$$

A Taylor expansion in α around the equilibrium position $\alpha = 0°$ (considering the expressions for α_{eff} and U_{eff} in Eq. (3)), then leads to a damped harmonic oscillator equation,

$$\ddot{\alpha} + \beta_{st}\dot{\alpha} + \omega_{st}^2\alpha = O(\alpha^3) \tag{5}$$

reminding of Eq. (1) with

$$\begin{cases} \omega_{st}^2 &= \dfrac{\rho S L U^2}{2J}\dfrac{\mathrm{d}C_{N_{st}}}{\mathrm{d}\alpha}\Big|_0 \\ \beta_{st} &= \dfrac{\rho S L^2 U}{2J}\dfrac{\mathrm{d}C_{N_{st}}}{\mathrm{d}\alpha}\Big|_0 = \dfrac{L}{U}\omega_{st}^2 \end{cases} \tag{6}$$

We note here that the pulsation of the quasi-static regime is given by the slope of the C_N coefficient at the origin. We expect the expansion around $\alpha = 0°$ to hold over the entire linear regime of $C_{N_{st}}$, *i.e.* up to the stall angle ($\alpha \sim 40°$, see Fig. 2a), which means that this approximation should hold for the observed relaxation dynamics after the first minimum for the signal shown in Fig. 2 (i.e. for $t > 1.2$ s). We also stress that the quasi-static modeling does not take into account the unsteadiness behavior due to vortex shedding and is thus expected to fail for the lowest values of the reduced velocity, as developed in the next section.

3. Results

Following the previous considerations, it is tempting to compare the measured weathercock relaxation dynamics towards equilibrium to the quasi-static damped oscillator dynamics associated to Eq. (5). Fig. 3 shows the experimental values for ω^2 and β (computed by fitting the experimental signals as a damped harmonic oscillator dynamics) as functions of their estimations using the static coefficient approximation ω_{st}^2 and β_{st} (Eq. (6)). It can be seen that, for the range of explored parameters, both the oscillating pulsation ω and the damping coefficient β are linearly related to the quasi-static predictions. The quasi-static damping coefficient β_{st} slightly underestimate the actual damping coefficient β, while the quasi-static estimate of the pulsation ω_{st} systematically overestimate the actual pulsation ω. This suggests that, although the quasi-static approximations ω_{st} and β_{st} give the correct order of magnitude for the oscillating frequency and damping, corrections to the quasi-static model are still required. The quasi-static values for the oscillating frequency and the damping coefficient can therefore be considered as a reasonable first order approximation, from which quantitative corrections are to be derived in the frame of a refined modeling of the weathercock dynamics. In the following, we propose two ways of recovering the experimental dynamics by extending the quasi-static dynamics given by Eq. (4), first in the context of a time-domain expansion, second by introducing an empirically determined dynamical normal drag coefficient $C_{N_{in}}$. According to Eq. (2), the corrections are expected to depend not only on the angular position α, but explicitly upon the time t and/or the higher time derivatives of $\alpha(t)$ (angular velocity and acceleration). In the following, we introduce such corrections that can be computed *a priori*, and we show that they only depend upon the reduced velocity Ur or the flow velocity U.

3.1. Time domain correction

We propose in this section a refinement of the quasi-static model accounting for possible non-stationary corrections that would be responsible for the deviations observed for the weathercock dynamics, in particular regarding the expected oscillation frequency. When such frequency shifts are observed in unsteady aerodynamics, a common theoretical approach is the addition of stiffness and mass to the dynamics equation, thus taking into account the effective global impact of vortex shedding on the free dynamics. We note that for a rotating system as the one investigated here, the equivalent of an added mass would correspond to an added moment of inertia.

This approach, widely used in vortex-induced vibration theory, assumes that the behavioral dynamics depends on the ratio between the vortex shedding frequency and the frequency of natural oscillation of the system. Non-stationary aerodynamic corrections are expected to be dominant when natural oscillations are rapid or comparable to vortex shedding, while a quasi-static approach should hold for slow oscillations. As already stated in Section 1, this competition between natural oscillations and vortex shedding is usually quantified by the reduced velocity Ur, a characteristic dimensionless number which characterizes the unsteadiness of the aerodynamic couplings:

$$\mathrm{Ur} \equiv \frac{1}{\mathrm{St}}\frac{f_{vs}}{f} = \frac{U}{df}, \tag{7}$$

where f_{vs} is the vortex shedding frequency, f the natural oscillation frequency of the structure in the wind and $\mathrm{St} = df_{vs}/U$ the Strouhal number.

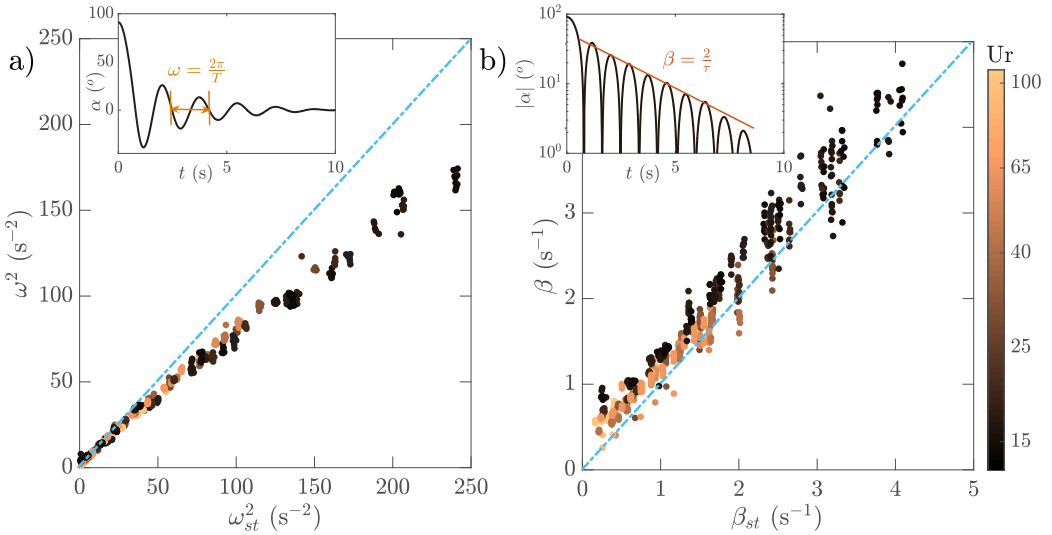

Fig. 3. (a) Experimental measured pulsation ω^2 with respect to the static estimated pulsation ω_{st}^2. (b) Experimental measured damping coefficient β with respect to the static estimated damping β_{st}. Dash-dotted lines represent identity and the color codes for the Ur parameter of each experiment on both graphs. (For interpretation of the references to color in this figure legend, the reader is referred to the web version of this article.)

In the present situation, as the weathercock is perfectly balanced, it has no structural natural oscillation frequency associated to its rotational dynamics (contrary to a weighted pendulum for instance). The linear relation between ω and ω_{st} shows indeed that the oscillation frequency has an aerodynamic origin, whose order of magnitude and trends are reasonably captured by the quasi-static Eq. (6). In the present case, the reduced velocity is therefore defined using the quasi-static oscillating frequency: $f = f_{st} \equiv \omega_{st}/2\pi$. This leads to the following expression for Ur:

$$\mathrm{Ur} = \frac{1}{\mathrm{St}}\frac{f_{vs}}{f} = \frac{U}{d}\frac{2\pi}{\sqrt{\frac{1}{2}\frac{\rho S U^2 L}{J}\left.\frac{\mathrm{d}C_N}{\mathrm{d}\alpha}\right|_0}} = \frac{4}{d^2}\sqrt{\frac{2\pi J}{\rho L\left.\frac{\mathrm{d}C_N}{\mathrm{d}\alpha}\right|_0}}. \tag{8}$$

Remarkably, Ur is found to be independent of the flow velocity U, linked to the fact that the natural oscillations of the balanced weathercock are self-induced by aerodynamic couplings. As such, Ur is varied in the experiments by the modifications of parameters d, J and L of the weathercock. The range of explored Ur in this study spans from 14 to 120 (see Table 1). We note that this broad range of accessible values of reduced velocity confirms that the observed oscillations of the weathercock are not primarily driven by vortex shedding, what would lead to values of $\mathrm{Ur} = \mathcal{O}(\mathrm{St}^{-1}) \simeq 10$ (since the Strouhal number for flat disks as investigated here is of order 10^{-1} (Gayout et al., 2021)). Vortex shedding is however expected to contribute to the observed deviations of the weathercock dynamics when compared to the quasi-static description. Modeling its contribution to the weathercock dynamics is the goal of this subsection.

In unsteady aeroelastic models, added mass, stiffness and damping are appended to the system dynamics equation in the simplest possible way, as additive linear corrections to the quasi-static equation Eq. (5), which becomes:

$$(1+m)\ddot{\alpha} + (\beta_{st} + \gamma U)\dot{\alpha} + (\omega_{st}^2 + k)\alpha = 0 \tag{9}$$

with m the added mass (added moment of inertia in the present case), γU the added damping and k the added stiffness, all normalized by the moment of inertia J. It follows that in the context of this refined model, the corrected predictions for the oscillation pulsation and damping coefficient are:

$$\begin{cases} \omega_{\mathrm{td}}^2 &= \dfrac{\omega_{\mathrm{st}}^2 + k}{1+m} \\ \beta_{\mathrm{td}} &= \dfrac{\beta_{\mathrm{st}} + \gamma U}{1+m} \end{cases} \tag{10}$$

Fig. 4 shows the three added parameters (k, m and γ) as functions of the reduced velocity Ur (the parameters are obtained by fitting the measured oscillation pulsation and damping with expressions (10)).

A similar behavior is observed for the three parameters: their values decrease as Ur increases. Numerical simulations at low Reynolds number reported the existence of $\mathrm{St} \simeq 0.07$ for subharmonic transverse vortex shedding for a disk (Gao et al., 2018). While the existence of a similar value for the Strouhal Number at larger Reynolds number is an open issue, a peak at

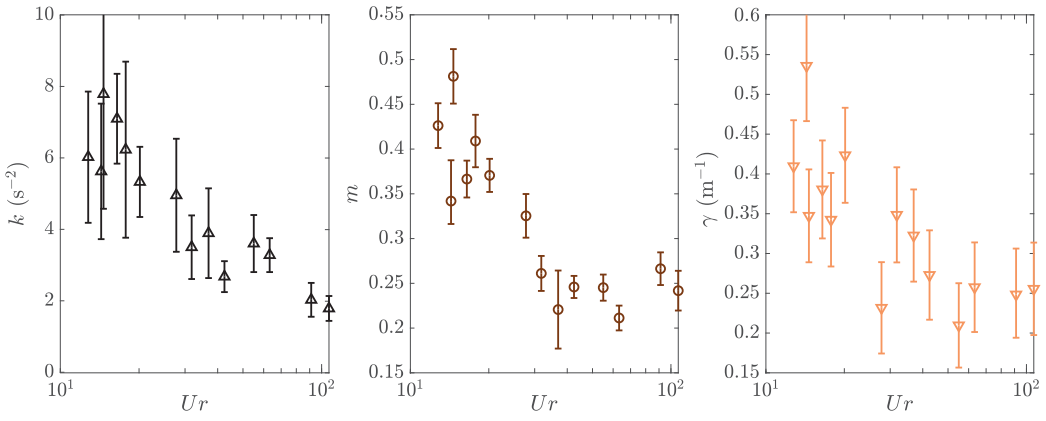

Fig. 4. Added stiffness k, mass m and damping γ obtained for each Ur parameter in the experiments. Dash-dotted line represents 1/St with St $\simeq$ 0.07.

Ur $\sim$ St^{-1} $\simeq$ 15 cannot be ruled out in the data shown in Fig. 4. The existence of a maximum for the corrections at Ur$\sim$ 15 would then be in agreement with the intuitive expectation that non-stationary corrections become preponderant when the oscillation frequency approaches that of vortex shedding. As expected these corrections then rapidly decrease as the reduced velocity increases (*i.e.* as the oscillation frequency becomes significantly smaller than vortex shedding frequency). The available data does not allow to be fully conclusive on whether the corrective parameters would decrease to zero as Ur keeps increasing or would tend to a finite, non-vanishing, asymptotic value. Hence, the quasi-static approximation is approached but not fully recovered even for Ur $\sim$ 100, while it is expected to hold in the limit Ur $\to \infty$. We cannot rule out the blade to be at the origin of these non-vanishing values of the added coefficients for Ur $\sim$ 100, especially since the largest values of Ur were probed using the smallest 3-cm diameter disk.

Another observation is that the maximum value of the added mass is close to 0.5, which reminds of the added mass coefficient found for a sphere immersed in fluid.

3.2. Empirically corrected C_N coefficient approach

We now investigate an empirical model, which, contrary to the previous approach, does not assume *a priori* a damped-harmonic oscillator behavior. It is indeed possible to empirically retrieve an instantaneous normal drag coefficient $C_N(\alpha_{\text{eff}}(t), t)$ using Eq. (4) and the experimental measurement of the angular dynamics of the weathercock.

The experimental instantaneous C_N coefficient is compared to its static equivalent $C_{N_{st}}$ computed from reported measurements for a fixed disk (Flachsbart, 1932) (dashed blue line) in Fig. 5(a), as a function of the effective angle of attack α_{eff}, shown here for $U > U^*$, U^* being defined in Eq. (11). Interestingly, the instantaneous $C_{N_{in}}$ recovers (after the first oscillation) a simple linear angular dependency, in the range $\alpha_{\text{eff}} \in [-40°; 40°]$, reminiscent of the linear region for the static coefficient $C_{N_{st}}$. We observe however that the slope of the linear region is strongly dependent on experimental conditions: it is consistently close to the static case for the lowest tested wind velocity U, but then systematically decreases when U is increased. This dependency on U is less pronounced on the initial oscillation starting at $\alpha = 90°$, although the global behavior on this part of C_N strongly deviates from the static behavior. This initial phase, which is strongly affected by the effects of stall, is out of the scope of the present study and shall be further explored in the future.

Another interesting observation is that the evolution of the ratio of the slope of the instantaneous $C_{N_{in}}(\alpha_{eff})$ coefficient to the slope of the static $C_{N_{st}}(\alpha_{eff})$ coefficient exhibits a $U^{-1/2}$ power as a function of the flow velocity U (see Fig. 5b).

Overall, these observations suggest that, in the range of interest ($\alpha_{eff} \in [-40°; 40°]$, i.e. after the first oscillation) a simple empirical correction to the quasi-static approach can be formulated using an effective instantaneous normal drag coefficient, with a linear angular dependency whose slope is related to the static case as:

$$\left.\frac{\mathrm{d}C_{N_{in}}}{\mathrm{d}\alpha}\right|_0 = \left(\frac{U^*}{U}\right)^{1/2} \left.\frac{\mathrm{d}C_{N_{st}}}{\mathrm{d}\alpha}\right|_0, \tag{11}$$

where the coefficient $U^* = U \left(\left.\frac{\mathrm{d}C_{N_{in}}}{\mathrm{d}\alpha}\right|_0 \Big/ \left.\frac{\mathrm{d}C_{N_{st}}}{\mathrm{d}\alpha}\right|_0 \right)^2 \simeq 3.7\,\mathrm{m\,s^{-1}}$ is obtained by the fit shown in Fig. 5(b). To better understand the effect of the corrected drag coefficient, we can consider the same linearization of Eq. (4) previously introduced for the quasi-static approximation and leading to Eq. (5), but using relation (11) as normal drag coefficient. The additional $U^{1/2}$ factor in C_N then modifies the linearized dynamics of Eq. (5) which now reads:

$$\ddot{\alpha} + \beta_{em}\dot{\alpha} + \omega_{em}^2\alpha = O(\alpha^3), \tag{12}$$

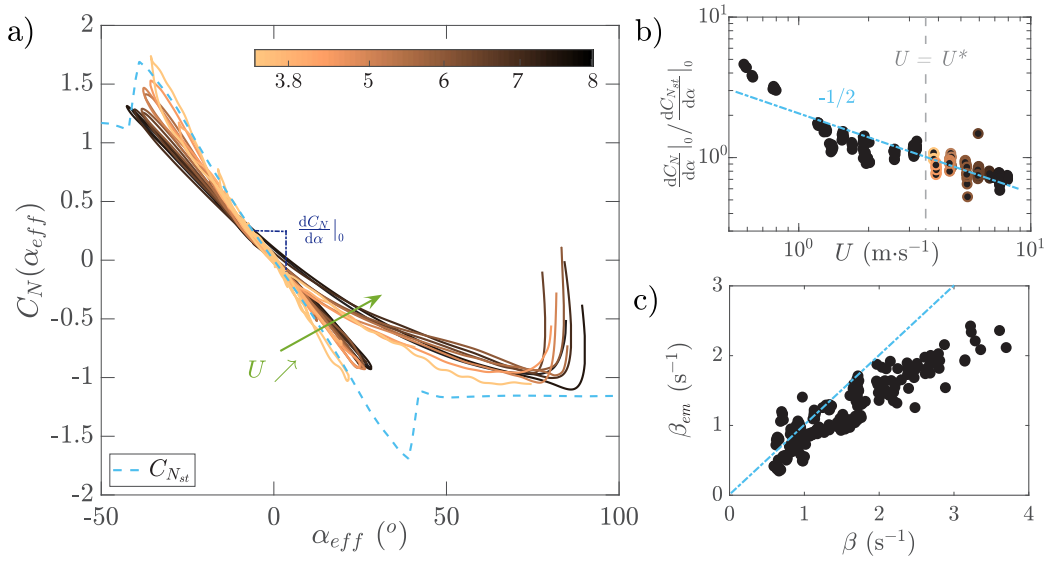

Fig. 5. (a) Dynamic (solid lines) vs static (dashed line) C_N coefficients as function of the angular position α_{eff} given by Eq. (3) for various flow velocities $U > U^*$. (b) Ratio between the slope of the dynamic $C_{N_{in}}$ coefficient and the static coefficient $C_{N_{st}}$ with respect to flow velocity. The value $U = U^*$ is highlighted with the dashed line. Color codes for the flow velocity $U > U^*$ similarly on (a) and (b). (c) Damping coefficient β_{em}, estimated from the empirical correction on the $C_{N_{st}}$ coefficient, compared to the experimental damping β. (For interpretation of the references to color in this figure legend, the reader is referred to the web version of this article.)

where ω_{em} and β_{em} are respectively the empirically predicted oscillation pulsation and damping:

$$\begin{cases} \omega_{em}^2 &= \omega_{\text{st}}^2 \left.\dfrac{\mathrm{d}C_{N_{in}}}{\mathrm{d}\alpha}\right|_0 \Big/ \left.\dfrac{\mathrm{d}C_{N_{st}}}{\mathrm{d}\alpha}\right|_0 \\ \beta_{em} &= \beta_{\text{st}} \left.\dfrac{\mathrm{d}C_{N_{in}}}{\mathrm{d}\alpha}\right|_0 \Big/ \left.\dfrac{\mathrm{d}C_{N_{st}}}{\mathrm{d}\alpha}\right|_0 \end{cases} \tag{13}$$

The damping coefficient β_{em} is plotted against the experimental damping coefficient in Fig. 5.(c), from which it is clear that an additional damping term is necessary to correctly describe the observed experimental dynamics. Remarkably, the strength of this additional damping is close to the added damping γU from the previous model (not shown here). While its origin is not clear, the strength of this additional damping as a function of d_{disk} is discussed further in Section 4.

4. Discussion

In this section, we briefly discuss possible physical interpretations of some of the additional parameters introduced to improve the non-stationary modeling of the weathercock dynamics and then compare the performances of the different modeling strategies (quasi-static, time-domain correction, empirical drag coefficient).

4.1. Physical interpretation of the modeling parameters

Let us first discuss the terms added in the model introduced in Section 3.1. In particular, the added mass (or added inertia) can be interpreted as the mass of fluid displaced and dragged by the disk during its motion. We can therefore compute the diameter d_{air} of an equivalent air sphere around the disk centered at the center of the disk and of moment of inertia mJ (we recall that m is normalized added moment of inertia):

$$d_{air}^3 \left(L^2 + \frac{d_{air}^2}{10} \right) = \frac{6\, mJ}{\pi \rho} \tag{14}$$

As shown in Fig. 6(a), this diameter d_{air} is almost linear in the diameter of the disk d_{disk} (with a plateau at the smaller values probably due to the influence of the rod holding the disk), consistent with the idea that larger disks drag a proportionally larger equivalent sphere of air.

Regarding the added damping in the time-domain corrected model, we define a corrective term $\epsilon = \frac{\gamma U}{\beta_{st}}$, such that $\beta_{\text{td}} = \beta_{\text{st}} \left(\frac{1}{1+m} + \epsilon \right)$. ϵ represents the correction required with respect to the quasi-static description, regardless of the added mass modification $\frac{1}{1+m}$ to the quasi-static damping. The evolution of ϵ as a function of the pendulum diameter

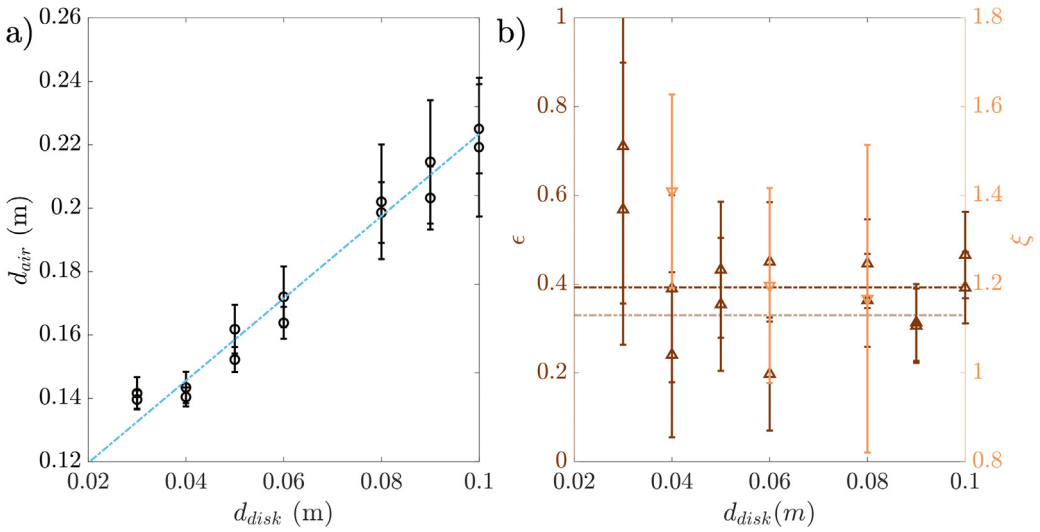

Fig. 6. Evolution of the interpreted added terms d_{air} (a), ϵ (b left axis) and ξ (b right axis) as functions of the diameter of the disk d_{disk}.

d_{disk} for each pendulum configuration is displayed in Fig. 6 (b). The value for the smaller disk is close to 0.7, and despite large error-bars, ϵ tends to converge at higher d_{disk} towards a constant value ϵ_c, represented by the dash-dotted lines.

Strikingly, a good candidate for this value is $\epsilon_c = \frac{\pi}{8}$ (dark line), which can be related to the damping of unsteady aerodynamic flutter models using potential flow theory (Fung, 2008; Blevins, 1990).

Let us now discuss the empirical model presented in Section 3.2. Fig. 5.c shows that the empirical damping β_{em} is lower than the experimentally observed damping β. It is convenient to introduce a multiplicative corrective factor $\xi = \beta/\beta_{em}$. The values of ξ computed for three configurations, selected for having the largest number of runs and largest number of total oscillations to minimize the systematic errors, are displayed in Fig. 6.(b), and are, as expected from Fig. 5.(c), always larger than unity. We note that this corrective factor on the damping is formally equivalent to the introduction of a correction on the relative velocity $L\dot{\alpha}$ in Eq. (3) and Fig. 1. A physical interpretation of this corrective factor would thus be an change of the relative velocity from $L\dot{\alpha}$ to $\xi L\dot{\alpha}$, resulting in modified effective parameters as:

$$\begin{cases} U_{\text{eff}}^{*2} &= U^2 + 2\xi LU\dot{\alpha}\sin(\alpha) + \xi^2 L^2\dot{\alpha}^2 \\ \alpha_{\text{eff}}^{*} &= \alpha + \arctan\left(\dfrac{\xi L\dot{\alpha}\cos(\alpha)}{U + L\xi\dot{\alpha}\sin(\alpha)}\right). \end{cases} \tag{15}$$

In this context, the dynamics of the weathercock now reads:

$$J\ddot{\alpha} = \frac{1}{2}\rho SLU_{\text{eff}}^{*2} C_{N_{st}}(\alpha_{\text{eff}}^{*}) \frac{\mathrm{d}C_{N_{in}}}{\mathrm{d}\alpha}\bigg|_0 \Big/ \frac{\mathrm{d}C_{N_{st}}}{\mathrm{d}\alpha}\bigg|_0$$

Though the uncertainty on the damping and empirical correction makes it difficult to be fully conclusive on the value of ξ and its trend, ξ being higher than 1 would mean that the air around the pendulum moves at a higher velocity than the pendulum its self. This could be explained by the fact that not only the air behind the pendulum is dragged away but the air ahead is deviated as well, and may induce a supplementary advection for the air behind.

4.2. Comparison of models

Here we aim explore the accuracy of the different modeling strategies (quasi-static, time-domain corrected, empirical C_N) in capturing the experimental behavior of the weathercock. We compare the solution of the modeling equations and the experimental signal for the same initial conditions as in the experiment ($\alpha(0) \simeq 90°$ and $\dot{\alpha}(0) \simeq 0\,°\,\text{s}^{-1}$). The corresponding signals are shown in Fig. 7 (a). To quantify the discrepancy between the experiment and the modeling we compute the quadratic angular error $\sqrt{\langle \Delta\alpha^2 \rangle}$ between the experimental signal and each of the models.

While the time-domain corrected model collapses almost perfectly on the experiment with $\sqrt{\langle \Delta\alpha^2 \rangle} \leq 2°$, the empirical C_N model happens to be quite wrong as $\sqrt{\langle \Delta\alpha^2 \rangle} \simeq 10°$. This is due to the lack of capacity the this model to reasonably reproduce the transient dynamics of the first oscillation, which is strongly impacted by the complex behavior of C_N when the disk passes the stall angle. The good capacity of the time-domain corrected model to reasonably capture this transient while the corrective model and coefficients (added inertia, damping and stiffness) have only been derived based on the linearized dynamics past the first oscillation, is striking. The static model exhibits a relatively small global deviation from the experimental signal, of about $\sqrt{\langle \Delta\alpha^2 \rangle} \simeq 5°$ only, despite the lack of fidelity in both frequency and damping.

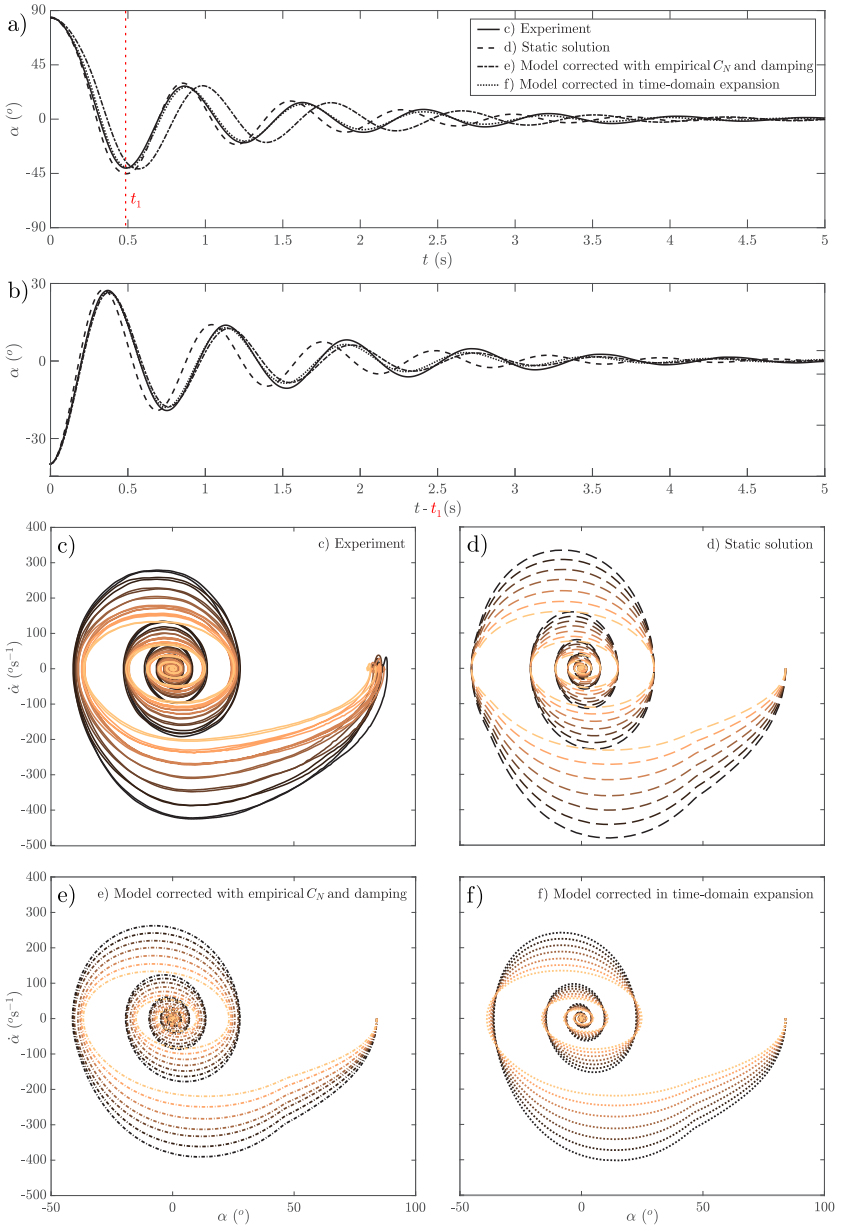

Fig. 7. Comparison between the experimental signal and the models with initial conditions (a) at the vertical and (b) at the first minima of oscillation. Phase portraits for the experiment and models: (c) experiment, (d) static coefficient model, (e) empirical dynamic coefficient model with added damping and (f) time-domain expansion model. The color codes for the flow velocity, with the lighter being the smaller velocity. All presented curves were obtained from the 4 cm weathercock with magnet attached, similar results were obtained for the other weathercocks. (For interpretation of the references to color in this figure legend, the reader is referred to the web version of this article.)

In order to ignore the impact of the transient dynamics, we have considered the situations where the initial condition is taken at the first minimum of oscillation (t_1), hence already past the stall angle and in the linear part of the C_N coefficient. The corresponding signals, both experimental and from the models, are shown in Fig. 7 (b) as a function of $(t - t_1)$. It can be seen that in that case, the time-domain corrected model and the empirical C_N model capture almost perfectly (with $\sqrt{\langle \Delta\alpha^2 \rangle} \simeq 1°$) the relaxing dynamics of the weathercock. The quasi-static dynamics is on the contrary at odds, indicating that the moderate error noted for the previously discussed initial conditions was fortuitous.

Finally, for a deeper insight into the dynamical fidelity of the modeling we consider the phase portraits (in $(\alpha, \dot{\alpha})$ space) of the weathercock dynamics (Fig. 7.c–f). From this point of view, while all models reasonably capture the qualitative behavior of the experiment, the match seems to be greater for the empirical C_N model, especially regarding the flow velocity dependence.

Hence to conclude, for small oscillations, the two models we propose in this paper to account for non-stationary aerodynamics correctly reconstruct the dynamics of the system. However if large oscillations are observed, the time-domain corrections transcribe better the behavior of stabilization, although further dedicated investigation focusing on the dynamics near stall would be required to clarify whether this is a reliable or a fortuitous observation.

5. Conclusion

We have presented two very different approaches to incorporate non-stationary effects into the static aerodynamic modeling of a relaxing weathercock made of a balanced pendulum composed of a flat disk at the end of a freely pivoting rod. Past the first oscillation, the weathercock dynamics was found to be well approximated by a damped harmonic oscillator behavior, hence characterized by its oscillation frequency and exponential damping coefficient. In the limit of small angles ($|\alpha| < 40°$) this dynamics is qualitatively retrieved by a simple quasi-static model considering only the (linear) angular dependency of the static normal drag coefficient $C_{N_{\mathrm{st}}}$ of a fixed inclined disk. This model reasonably captures the qualitative dynamics, but fails capturing the accurate values for the oscillation frequency and damping coefficient. The deviations increase as the frequency of oscillation increases, hence suggesting that non-stationary aerodynamics effects must be considered to accurately model these situations.

To do so, we have first considered a time-domain corrected approach, where effects of non-stationarity are modeled based on added moment of inertia, added damping and added stiffness. Our results show that the importance of these corrections increases when the reduced velocity Ur (which in our case does not depend on the wind-speed and is entirely defined by the weathercock geometry) decreases and approaches a value close to the inverse St^{-1} of the Strouhal number associated to transverse vortex shedding, suggesting a strong coupling between shedding and oscillations of the weathercock in such conditions. As Ur increases, the non-stationary corrections decrease, and remain finite even for $\mathrm{Ur} \sim 10\mathrm{St}^{-1}$ hence pointing that even at high values of Ur (*i.e.* when oscillations are slow compared to vortex shedding the effective normal drag coefficient to be considered for a quasi-statically freely rotating disk may still deviate from the case of fixed disk.

As a second modeling strategy of the weathercock dynamics, we have introduced an empirically determined instantaneous normal drag coefficient. Our results suggest that, in the angular region of interest ($|\alpha| < 40°$) this instantaneous drag coefficient follows the same angular dependency as the static drag coefficient, but that a velocity dependent factor should be introduced. This factor was found to scale as $(U^{1/2})$ possibly pointing to a possible role played by skin friction effects, although future studies would be required to gain insight into this observation. The comparison of the performances of the two modeling strategies with respect to the experimentally measured weathercock dynamics shows that in the linear region ($|\alpha| < 40°$), both models very accurately reproduce the motion of the weathercock. Interestingly, the time-domain corrected model also behaves reasonably well beyond the linear domain for which it has been built, in particular when the weathercock passes by the static stall angle, a transient that the empirical C_N model fails to capture. Whether the good behavior of the time-domain corrected model in this transient is real or fortuitous would require further dedicated studies around the stall angle.

CRediT authorship contribution statement

Ariane Gayout: Conception and design of study, Acquisition of data, Analysis and/or interpretation of data, Writing – original draft, Writing – review & editing. **Ármann Gylfason:** Conception and design of study, Analysis and/or interpretation of data, Writing – original draft. **Nicolas Plihon:** Conception and design of study, Analysis and/or interpretation of data, Writing – original draft, Writing – review & editing. **Mickaël Bourgoin:** Conception and design of study, Analysis and/or interpretation of data, Writing – original draft, Writing – review & editing.

Declaration of competing interest

The authors declare that they have no known competing financial interests or personal relationships that could have appeared to influence the work reported in this paper.

Data availability

Data will be made available on request.

Acknowledgments

The authors acknowledge financial support of the Project IDEXLYON of the University of Lyon in the framework of the French Programme Investissements d'Avenir (ANR-16-IDEX-0005) and of the Laboratoire de Physique for the upgrade of the wind-tunnel. The authors warmly thank J. Borée, Y. Haffner and C. Sicot for stimulating discussions. All authors approved the version of the manuscript to be published.

References

Allen, J., Smits, A., 2001. Energy harvesting eel. J. Fluids Struct. 15 (3–4), 629–640. http://dx.doi.org/10.1006/jfls.2000.0355.

Berhault, J., 1977. Wind noise in buildings. Wind Eng. 1 (1), 67–82, https://www.jstor.org/stable/43749065.

Blevins, R.D., 1990. Flow-Induced Vibration. Van Nostrand Reinhold.

Brunton, S.L., Rowley, C.W., 2013. Empirical state-space representations for Theodorsen's lift model. J. Fluids Struct. 38, 174–186. http://dx.doi.org/10.1016/j.jfluidstructs.2012.10.005.

Brunton, S.L., Rowley, C.W., Williams, D.R., 2013. Reduced-order unsteady aerodynamic models at low Reynolds numbers. J. Fluid Mech. 724, 203–233. http://dx.doi.org/10.1017/jfm.2013.163.

Chiereghin, N., Cleaver, D.J., Gursul, I., 2019. Unsteady lift and moment of a periodically plunging airfoil. AIAA J. 57 (1), 208–222. http://dx.doi.org/10.2514/1.J057634.

Corke, T.C., Thomas, F.O., 2015. Dynamic stall in pitching airfoils: aerodynamic damping and compressibility effects. Annu. Rev. Fluid Mech. 47 (1), 479–505. http://dx.doi.org/10.1146/annurev-fluid-010814-013632.

Fegeant, O., 1999a. Wind-induced vegetation noise. Part I: A prediction model. Acustica 85 (2), 228–240.

Fegeant, O., 1999b. Wind-induced vegetation noise. Part II: Field measurements. Acustica 85 (2), 241–249.

Flachsbart, O., 1932. Messungen an ebenen und gewölbten Platten. In: Ergebnisse der Aerodynamischen Versuchsanstalt zu Göttingen - IV. Lieferung. Verlag von R. Oldenburg, München und Berlin, pp. 96–100.

Fung, Y.C., 2008. An Introduction to the Theory of Aeroelasticity. In: Dover Books on Aeronautical Engineering, Dover Publications.

Gao, S., Tao, L., Tian, X., Yang, J., 2018. Flow around an inclined circular disk. J. Fluid Mech. 851, 687–714. http://dx.doi.org/10.1017/jfm.2018.526.

Gayout, A., Bourgoin, M., Plihon, N., 2021. Rare event-triggered transitions in aerodynamic bifurcation. Phys. Rev. Lett. 126 (10), 104501. http://dx.doi.org/10.1103/PhysRevLett.126.104501.

Haddadpour, H., Firouz-Abadi, R., 2006. Evaluation of quasi-steady aerodynamic modeling for flutter prediction of aircraft wings in incompressible flow. Thin-Walled Struct. 44 (9), 931–936. http://dx.doi.org/10.1016/j.tws.2006.08.020.

Lu, Z., Wen, Q., He, X., Wen, Z., 2019. A flutter-based electromagnetic wind energy harvester: Theory and experiments. Appl. Sci. (Switzerland) 9 (22), http://dx.doi.org/10.3390/app9224823.

McCroskey, W.J., 1982. Unsteady airfoils. Annu. Rev. Fluid Mech. 14 (1), 285–311. http://dx.doi.org/10.1146/annurev.fl.14.010182.001441.

Obligado, M., Puy, M., Bourgoin, M., 2013. Bi-stability of a pendular disk in laminar and turbulent flows. J. Fluid Mech. 728, R2. http://dx.doi.org/10.1017/jfm.2013.312.

Olivieri, S., Boccalero, G., Mazzino, A., Boragno, C., 2017. Fluttering conditions of an energy harvester for autonomous powering. Renew. Energy 105, 530–538. http://dx.doi.org/10.1016/j.renene.2016.12.067.

Peters, D., 2008. Two-dimensional incompressible unsteady airfoil theory—An overview. J. Fluids Struct. 24 (3), 295–312. http://dx.doi.org/10.1016/j.jfluidstructs.2007.09.001.

Taha, H.E., Hajj, M.R., Beran, P.S., 2014. State-space representation of the unsteady aerodynamics of flapping flight. Aerosp. Sci. Technol. 34, 1–11. http://dx.doi.org/10.1016/j.ast.2014.01.011.

Tavallaeinejad, M., Salinas, M.F., Païdoussis, M.P., Legrand, M., Kheiri, M., Botez, R.M., 2021. Dynamics of inverted flags: Experiments and comparison with theory. J. Fluids Struct. 101, 103199. http://dx.doi.org/10.1016/j.jfluidstructs.2020.103199.

Theodorsen, T., 1935. General Theory of Aerodynamic Instability and the Mechanism of Flutter. Tech. Rep. TR 496, NACA.

Truong, K.V., Tobak, M., 1990. Indicial response approach derived from Navier-Stokes equations. Part 1: Time-invariant equilibrium state. Tech. Rep. Technical Memorandum 102856, NASA.

von Kármán, T., Sears, W.R., 1938. Airfoil theory for non-uniform motion. J Aeronaut. Sci. 5 (10), 379–390. http://dx.doi.org/10.2514/8.674.

Wagner, H., 1925. Über die Entstehung des dynamischen Auftriebes von Tragflügeln. ZAMM - J. Appl. Math. Mech./Z. Angew. Math. Mech. 5 (1), 17–35. http://dx.doi.org/10.1002/zamm.19250050103.

Wu, N., He, Y., Fu, J., Liao, P., 2021. Performance of a bistable flow-energy harvester based on vortex-induced vibration. J. Wind Eng. Ind. Aerodyn. 217, 104733. http://dx.doi.org/10.1016/j.jweia.2021.104733.